AIMS Materials Science, 8(5): 776–791.
DOI: 10.3934/matersci.2021047
Received: 13 September 2021
Accepted: 19 October 2021
Published: 26 October 2021

http://www.aimspress.com/journal/Materials

Research article

Lateral growth of xenon hydrate films on mica

Avinash Kumar Both and Chin Li Cheung*

Department of Chemistry, University of Nebraska-Lincoln, Lincoln, NE 68588, USA

* **Correspondence:** Email: ccheung2@unl.edu; Tel: +1-402-472-5172.

Abstract: In this paper, we report an *in situ* optical microscopy study of lateral growth of xenon (Xe) hydrate thin films on mica at sub-zero temperatures. The interactions between a solid surface and water molecules can strongly affect the alignment of water molecules and induce ice-like ordered structures within the water layer at the water-surface interface. Mica was chosen as a model surface to study the surface effect of hydrophilic sheet silicates on the lateral growth of Xe hydrate films. Under the experimental conditions, the lateral growth of Xe hydrate films was measured to be at an average rapid rate of ~200 μm/s and 400 μm/s under two different pressures of Xe. Mass transfer estimation of the Xe-water system revealed that the increasing trend of lateral film growth rates followed the increase in the net mass flux and aqueous solubility of Xe. However, as the supercooling temperature increased, the trend of lateral film growth rates attained a plateau region where little change in the rate was observed. This unique feature in the lateral film growth trend, the fast lateral growth kinetics, and the short induction time for hydrate film growth hinted at the assistance of the mica surface to aid the lateral growth process of Xe hydrate films at low Xe mass flux and at a low degree of subcooling. A mechanism based on the reported structured water layer at the interface on mica was proposed to rationalize a postulated surface-promotional effect of mica on the nucleation and lateral growth kinetics of Xe hydrate films.

Keywords: gas hydrate; hydrate film; clathrate; mica; Xenon; interfaces

1. Introduction

Gas hydrates (or clathrate hydrates) are crystalline, water-based compounds stabilized by a robust three-dimensional hydrogen-bonded network of water molecules (called hydrate cages) and entrapped with guest gas molecules in these cages [1,2]. These unique properties have enabled gas hydrates to have potential applications in technologies for transportation and storage of methane

(CH_4), carbon sequestration, and water desalination [3]. On Earth, a significant amount of CH_4 hydrate is buried in the ocean floor, the permafrost region, and the polar caps [4]. The extra-terrestrial existence of gas hydrates is unknown, but many theoretical studies in the past decades have hypothesized the existence of different gas hydrates in extraterrestrial environments such as Mars and Titan (Saturn's biggest satellite) [5,6]. Thus, besides the beneficial development of energy-related applications [7], resolving the formation dynamics of gas hydrates could also reveal critical information about the cosmochemical footprint of the solar system and the astrophysical origin of various heavenly bodies [8].

In recent years, xenon (Xe) hydrate has emerged as a lucrative hydrate system for investigating different aspects of the hydrate growth process and hydrate applications due to its conveniently attainable formation conditions (such as at −1 °C and under 1.5 bar) [9,10]. For example, Xe hydrate has been applied as a model system to study various aspects of CH_4 hydrate growth processes which typically require high pressure of methane and low temperature [9]. In addition, Xe hydrates have been studied with emphasis on their potential application in cryopreservation technology [10,11]. Furthermore, since Xe is a primordial noble gas, the concentration ratios of Xe and its isotopes in the atmosphere of different planets and satellites can provide clues about the astrophysical evolution of different heavenly objects and their atmosphere [12]. Among the geoscience community, there is a current scientific inquiry called the "missing xenon paradox", that addresses the deficiency of Xe in the atmospheres of Earth, Venus, Pluto, Mars, and Titan [13]. Many hypotheses have been proposed to justify this lack of Xe, ranging from Xe being trapped within ice polymorphs in the form of Xe hydrates to Xe forming compounds with different minerals within the core or crust of heavenly objects [14]. Hence, though the structures of Xe hydrates and the growth process of its bulk phase have been methodologically studied since the 1990s, investigations of the initial growth process of Xe hydrates under different conditions and types of the environment have continued to attract interests among researchers especially from the chemistry, chemical engineering, and planetary science communities.

Identifying factors that control the dynamic growth of hydrates is of fundamental importance to both their utilization as an energy resource and their inhibition in flow assurance and workover operations [15]. Most of the hydrate formers (guests) are not soluble in water [16]. The formation process of gas hydrates consists of three phases: nucleation, film growth, and bulk growth. Gas hydrates initially form as a thin crystalline porous film at the gas-water interface [17]. As the interface between the water phase and the solid support, a surface can play a key factor in influencing the nucleation and growth of gas hydrate films [18,19]. It has been reported that surfaces can change the gas distribution and local organization of water molecules near the liquid-solid interfaces [20]. This surface-induced ordering inhibits the ability of water molecules to interact with neighboring water molecules as in the bulk state and thus may result in a different liquid density at the interface as compared to the bulk liquid [21]. The interactions arising from the different arrangements of H-bonded water molecules together with the surface wettability and adhesion can dictate the orientation of the water molecules near the water-surface interface, which in turn can significantly affect the nucleation and growth dynamics of gas hydrates [20]. For instance, on Earth, CH_4 hydrates are naturally affected by solid surfaces arising from rocks, biomass, and geological sediments [22]. Silicate minerals are common rock-forming minerals made up of silicate groups. They constitute approximately 90% of Earth's crust [23]. Silicates may exist as stardust in many meteorites [24] and interplanetary dust [25] within the solar system. However, most studies of gas

hydrate growth on silicates were performed to study the bulk growth rather than the film growth. Hence, gas hydrate film growth studies on different silicate mineral or simulant model surfaces are occasionally reported.

Mica is one ideal surface model for studying how water-solvated surfaces can influence the growth and nucleation of gas hydrates [26]. It belongs to a group of sheet silicate (phyllosilicates) minerals [26]. The water-mica interface has been extensively explored to study fluid dynamics in nanofluidics, lubrication condition in tribology, diffusion-adsorption processes in biological systems [27]. Additionally, studies of water forming an ice-like two-dimensional H-bonded network to the surface of mica have been reported by first-principles molecular dynamics (MD) simulations [28]. In the MD simulation, the interfacial water molecules were demonstrated to have a preferential alignment of hydrogen donor bonds with the basal oxygen atoms present on the surface of mica [28]. This resulted in the formation of a water monolayer on mica without any dangling hydroxyl (OH) groups and a net dipole moment with the positive end aiming towards the surface of mica. This ice-like arrangement of interfacial water molecules has been experimentally verified through Kelvin probe microscopy [29], vibration sum-frequency spectroscopy [30], and high-resolution X-ray reflectivity [31]. These experimental studies also did not detect any freely dangling OH groups and the surface potential of mica was observed to decrease upon water adsorption. These results agreed with the MD simulation's finding, suggesting possible influences of these oriented water structures on the formation of hydrate structures on mica.

Herein, we report our study of the lateral growth dynamics of Xe hydrate films on mica for extending the studies of hydrate film formation at the water-gas interface in presence of a solid surface. *In situ* optical microscopy was applied to experimentally measure the lateral growth rates of Xe hydrate films propagating across the gas-water interface on mica at sub-zero temperatures. The properties of the hydrate films and their lateral growth process at the interface between the water phase and the hydrate former (guest) phase are of importance to understand the overall kinetics of the hydrate formation process. When water comes in contact with Xe under pressure and low-temperature environments, Xe hydrate forms a film at the water-xenon interface [32]. In the initial stage, this film grows laterally to cover the surface of the substrate while at the same time grows in thickness to approach the bulk growth stage. The lateral growth kinetics of Xe hydrate films depend on the heat transfer from the vicinity of the hydrate film front. Several thermodynamic factors, including the equilibrium temperature at the experimental pressure (T_{eq}), the degree of super pressure (ΔP_{sup}), and the degree of subcooling (ΔT_{sub}), are essential description factors to predict the formation of bulk Xe hydrates. Thus, the relationships between the lateral film growth rate and these thermodynamic factors (T_{eq}, ΔP_{sup}, and ΔT_{sub}) were determined to gain thermodynamic insights into the influence of the mica surface on the lateral growth process of Xe hydrate films. Mass transfer of Xe to the water films and the solubility of Xe in the water films were also estimated to reveal their correlation with the measured lateral film growth rates. To our best knowledge, the lateral growth dynamics of Xe hydrate films on mica have not been reported.

2. Materials and methods

2.1. Apparatus and materials

The lateral growth dynamics of Xe hydrate films were monitored and recorded with an

Olympus SZ-STS optical microscope (Olympus Life Science, Center Valley, PA) equipped with a CCD camera and a computer (Figure 1 and Figure S1 in the supplementary). Sheets of ruby muscovite mica (Ted Pella, Inc., Redding, CA) were cut into circular discs of 1-cm diameter using a hole-puncher (Figure S2a). The chemical composition of the mica substrates for the Xe hydrate growth was listed in Table S1 of the supplementary. A temperature-controlled microscope stage (THMS600-PS, Linkam Scientific Co. Ltd., Tadworth, UK) was used as a mini reactor for growing Xe hydrate (Figure S2b,c). Nanopure water with 18.2 MΩ·cm resistivity was acquired from a Synergy water filtration system (VWR, Radnor, PA). UHP grade Xe (Praxair, Inc., Danbury, CT) was used as the Xe source to synthesize the Xe hydrate films. Confocal micro-Raman microscopy was performed using a DXR Raman microscope (Thermo Fisher Scientific, LLC, Waltham, MA) with the Linkam microscopy stage for identifying the water films and the Xe hydrate films on mica. The Raman analysis was carried out using a 532 nm laser with 2 mW power and a 0.25 μm pinhole aperture. The CSMGem [33] software was applied to determine the Xe composition (mole fraction of Xe) at different experimental temperatures (T_{exp}) and pressures (P_{exp}) in the aqueous (Xe and H_2O) system.

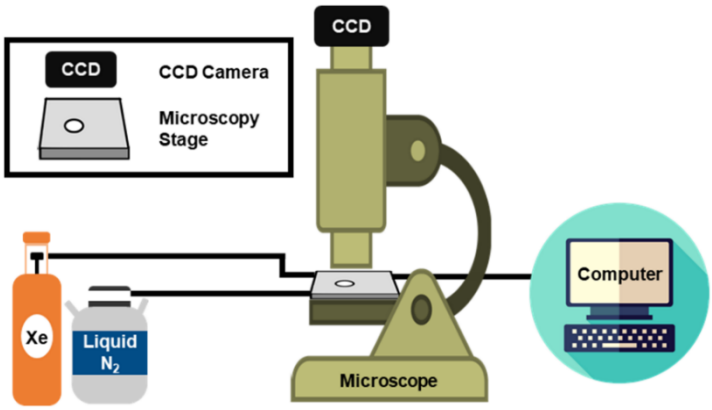

Figure 1. Schematic of the experimental setup for studying the lateral growth of Xe hydrate films.

2.2. Synthesis of Xe hydrate films

In an experiment to synthesize Xe hydrate films, nanopure water was first sprayed from an atomizer to form a water film on a freshly cleaved mica disc substrate of 1 cm in diameter. The water-coated substrate was placed on a quartz crucible on the platform of a temperature-controlled microscope stage located under the microscope imaging system. The stage was then sealed closed, purged with Xe for two minutes, and pressurized with Xe up to 2.75 bar (275.79 kPa) or 3.45 bar (344.73 kPa). Even though Xe hydrate can form at 1.5 bar [34], higher pressure and low temperature were chosen to ensure a shorter induction time [15] to form Xe hydrate. Afterward, the temperature of the substrate was lowered to the experimental temperature (T_{exp}) at a cooling rate of 5 K per minute for studying the lateral growth of Xe hydrate films at sub-zero temperatures. T_{exp} ranging from 268.13 K and 253.13 K were selected to study the hydrate film growth. After reaching the set temperature, the lateral film growth processes were visually observed under the optical microscope and the growth videos were recorded on a computer. Note that we only focused on analyzing the lateral film growth data from experiments in which the water films on mica never turned into ice and

always remained in a super-cooled state before the growth of Xe hydrate films.

2.3. Analysis of lateral Xe hydrate film growth on mica

The growth and the nucleation of crystalline Xe hydrate were observed to be stochastic processes [35]. Once the Xe hydrate started to form at the water-Xe interface, the Xe hydrate films grew rapidly alongside the edge of the gas-water interface and assembled into an advancing thin, porous film [36]. The lateral growth rates of Xe hydrate films at different experimental temperatures (T_{exp}) were determined by evaluating the width of the initial lateral film growth "step" as a function of time from the growth videos and fitting the plots of the width of advancing growth steps vs. growth time with a linear function to yield the slopes (lateral growth rates). The initial lateral growth rates of Xe hydrate films appeared to be constant. The relationships between the lateral growth rate of the hydrate film and several thermodynamic factors including the experimental temperature (T_{eq}), the superpressure (ΔP_{sup}), and the subcooling temperature (ΔT_{sub}) were also determined in our hydrate film growth analysis. T_{eq} indicates the equilibrium temperature at the experimental pressure (P_{exp}). It regulates the kinetics of the lateral hydrate film growth and the transport processes near the hydrate growing site. It was calculated using the Clausius–Clapeyron equation [37]. ΔP_{sup} symbolizes the degree of superpressure, which is the difference between P_{exp} and the equilibrium pressure (P_{eq}) at the experimental temperature (T_{exp}) (or $\Delta P_{sup} = P_{eq} - P_{exp}$). ΔP_{sup} provides information about the mass transfer of Xe gas to a Xe hydrate growing site. ΔT_{sub} indicates the degree of subcooling which is defined as the difference between T_{exp} and T_{eq} at P_{exp} (or $\Delta T_{\text{sub}} = T_{eq} - T_{exp}$). Thus, it is regarded as an index of the heat transfer process.

3. Results and discussion

3.1. Observations of lateral Xe hydrate film growth

The lateral growth dynamics of Xe hydrate films on mica were observed at temperatures ranging from 268.13 to 253.13 K and under two pressures of Xe (2.75 bar and 3.45 bar) through *in situ* optical microscopy. In our experiments and other reported hydrate film growth studies [36], the gas hydrate films were typically assumed to nucleate and grow along at the gas-water interface (Figure 2). Confocal Raman microscopy was employed to characterize Xe hydrate films and identify their formation locations by studying the OH vibration region around 3000 cm^{-1} to 3500 cm^{-1} of the samples' Raman spectra (Figure S3). The Raman spectrum of a Xe hydrate film typically displays a characteristic OH peak at around 3100 cm^{-1}, matching up the reported values of Xe hydrate. The asymmetric shape of this shoulder peak also corresponds well to the Raman data of other similar gas hydrate structures [17,38,39]. In contrast, the Raman spectrum of a water film displays the OH peak as a broad peak in the 3000 cm^{-1} to 3500 cm^{-1} region due to the flexible network of water molecules in liquid [40]. According to the Raman analysis of our samples, Xe hydrate films typically appeared to have a grey color whereas the supercooled water films appeared as clear under the microscope in our study.

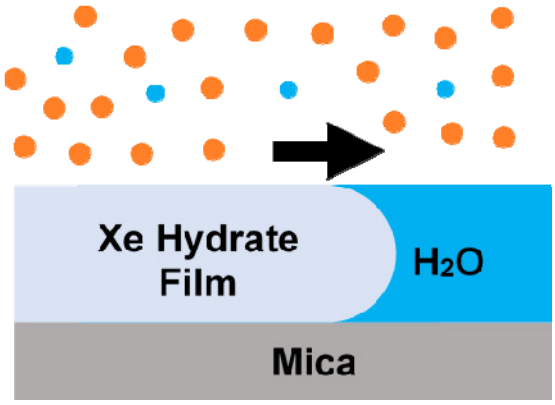

Figure 2. Illustration of the profile of lateral Xe hydrate film growth at the gas/liquid interface. Orange dots: Xe atoms; blue dots: H_2O molecules.

Under our experimental conditions, the initial lateral growth rates of Xe hydrate films on mica were measured by microscopic video analysis and were found to range from 10's to almost 1000 μm/s. For example, Figure 3 and Video SV1 in supplementary show a typical formation of a Xe hydrate film on mica across the viewing window (~550 μm × 420 μm) under 2.75 bar of Xe. The growth fronts of hydrate films were usually observed to have micron-sized roughness. However, the degree of subcooling from the chosen conditions provided sufficient driving force such that steps and kinks on the mica surface were not observed to cause pinning on the hydrate growth front (Video SV1 in supplementary). In general, the hydrate film growth rates were found to be fast in comparison to other reported hydrate films [41]. The average lateral film growth rates measured under the two Xe pressure conditions (2.75 bar and 3.45 bar) were approximately 200 and 400 μm/s, respectively (Figure 4). Note that the induction time [15] to form a Xe hydrate film along with the Xe-water interface in our study was usually between 25 and 40 s. This was also much faster than the induction time of other reported gas hydrate films (such as methane hydrates [41] and other alkane hydrates [36]) which were observed in the order of minutes to hours.

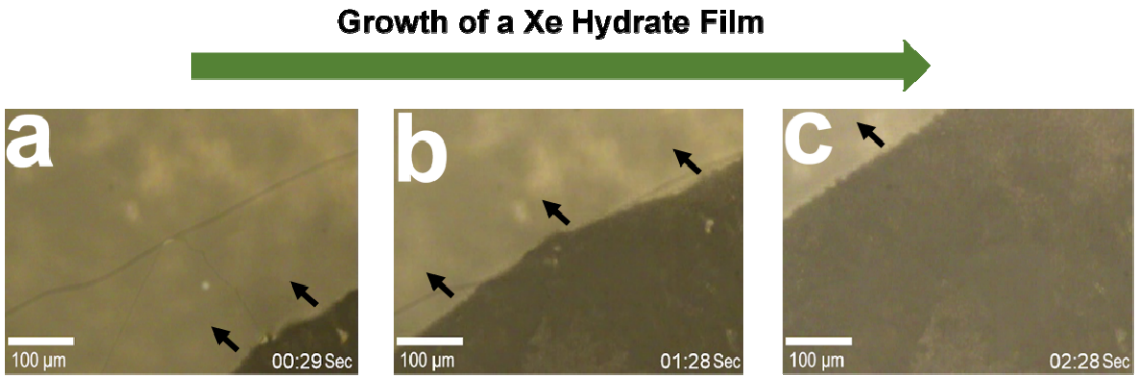

Figure 3. Chronological illustrations depicting the lateral growth of a Xe hydrate film on mica following a cooling cycle at 263.13 K under 2.75 bar of Xe at growth time: (a) t = 0:29 s, (b) t = 1:28 s, and (c) t = 2:28 s.

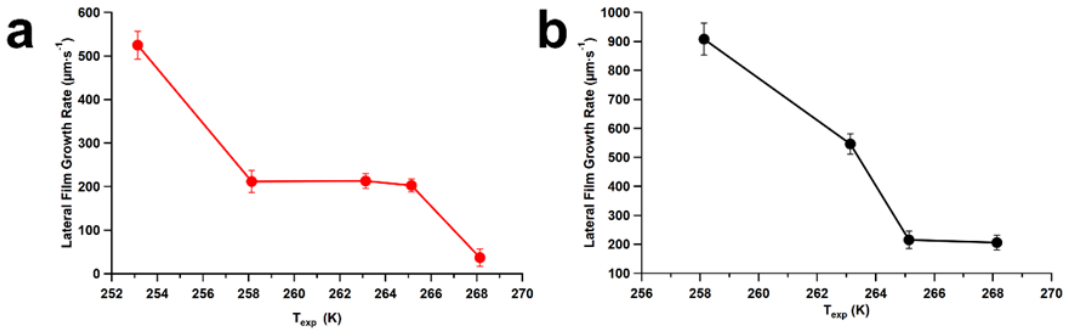

Figure 4. Plots of lateral film growth rates of Xe hydrate films on mica vs. experimental temperature (T_{exp}) under (a) P_{exp} = 2.75 bar and (b) P_{exp} = 3.45 bar of Xe. Each error bar indicates one standard deviation of the measurements.

Under sub-zero temperatures, as the experimental temperature increased, the rate of lateral hydrate film growth was found to decrease and unexpectedly reach a plateau with little decrease in the temperature before it further considerably declined (Figure 4). For example, the plateau region was apparent (258.13 to 265.13 K) under 2.75 bar of Xe (Figure 4a) while it was vaguely noticeable (from 265.13 to 268.13 K) under 3.45 bar of pressure in Xe (Figure 4b). Since gas hydrates had high heat of formation [42], the general trend of increasing lateral growth rate with decreasing growth temperature agreed well with the presumption from thermodynamics arguments. However, the plateau regions with a temperature range of more than a few Kelvins under both pressure conditions were not initially anticipated.

3.2. Mass transfer processes: Net mass flux and aqueous solubility of Xe

The mass transfer rates of Xe were studied to evaluate the formation of Xe hydrate [41]. Since the lateral film growing phase was assumed at the hydrate film-forming edge immersed in a water film (Figure 2), the nucleation and formation of Xe hydrate were largely dictated by the mass flux of Xe to the water film and the solubility of Xe in the water film at the phase boundary of the Xe-H_2O system [9]. In general, the high net mass flux of the guest gas that has high aqueous solubility would be expected to yield faster hydrate film-growth kinetics [15]. In our study, the net mass flux of Xe gas to the Xe hydrate growth site was estimated using the kinetic theory of gases, in which the gas molecules were assumed to be an ideal gas, and the net mass flux [41] of gas molecules, ∅, was expressed as Eq 1:

$$\emptyset = \frac{\Delta P_{sup}}{\sqrt{2\pi m k T_{exp}}} \quad (1)$$

where ΔP_{sup}, m, k, and T_{exp} denote the degree of superpressure of Xe, the mass of a Xe atom, Boltzmann constant, and experimental temperature, respectively. As the formation and the decomposition of a Xe hydrate film were dynamic processes happening at the lateral film growth front, there were two mass fluxes of Xe: (a) away from and (b) toward the growth sites of the hydrate. Hence, the net mass flux to the growth sites was expressed using ΔP_{sup} ($\Delta P_{sup} = P_{eq} - P_{exp}$). For

example, we computed the net mass fluxes of Xe under 2.75 bar and 3.45 bar (Figure 5a) of Xe and plotted them against the experimental temperatures. In the sub-zero temperature range, the computed net flux of Xe increased by ~1.5 times with a decrease by 15 K in experimental temperature. To correlate this observed trend, we also calculated the solubility of Xe in the aqueous films at 2.75 bar and 3.45 bar of Xe. Within the range of experimental temperatures, the mass flux values corresponding to 2.75 bar (2–3 × 10^{-27} kg·m^{-2}·s^{-1}) were significantly lower than those of the mass flux corresponding to 3.45 bar (3–4 × 10^{-27} kg·m^{-2}·s^{-1}). This increase in net flux was due to the direct proportionality of the mass flux with the applied pressure. The CSMGem [33] software was applied to determine Xe composition (mole fraction of Xe) at different experimental temperatures (T_{exp}) and pressures (P_{exp}) in the aqueous (Xe and H_2O) system. The calculated mole fraction of Xe in aqueous media (or hydrate films) was plotted against the experimental temperatures (T_{exp}) (Figure 5b).

Our results showed that the mole fraction of Xe in the Xe·H_2O system increased by over ca. 2 times as the temperature decreased by 15 K under both pressures. These two trends indicated that the net flux of Xe was positively correlated to the mole fraction of Xe in the aqueous films. As the experimental temperature decreased, the net mass flux of Xe to a substrate would be expected to increase and more Xe could be incorporated in the Xe hydrate films, corroborating the general trend of faster lateral hydrate film growth rates observed in our experiments.

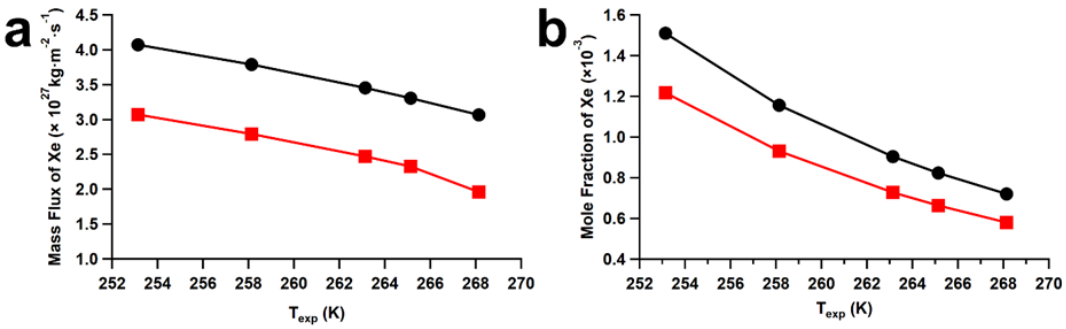

Figure 5. Plots of (a) mass flux of Xe to a water film vs. T_{exp} and (b) mole fraction of Xe within an aqueous film vs. T_{exp}. The solid squares and circles correspond to P_{exp} = 2.75 bar and P_{exp} = 3.45 bar of Xe respectively.

3.3. Analysis of lateral Xe hydrate film growth on mica

The lateral growth of Xe hydrate films on mica was examined by evaluating the relationships between the measured lateral growth rates of Xe hydrate films (v_f) and the corresponding thermodynamic driving force values (ΔT_{sub} and ΔP_{sup}) under the two different Xe pressure conditions. ΔT_{sub} was defined as $\Delta T_{sub} = T_{eq} - T_{exp}$, where T_{exp} was the initial experimental temperature for hydrate film growth and Teq was the equilibrium formation temperature of hydrate at the initial experimental pressure calculated using the hydrate model by Fray et al. [37]. We used the Eq 2 form of the Clausius–Clapeyron equation to compute the T_{eq} values:

$$ln\, P = A + \frac{B}{T} \tag{2}$$

where P is in pascal (Pa), T is in kelvin (K), A = 16.62 and B = −3159 for Xe gas [37]. ΔP_{sup} was computed as discussed in section mass transfer processes: Net mass flux and aqueous solubility of Xe.

The plots of measured lateral film growth rates against ΔT_{sub} (Figure 6) and ΔP_{sup} (Figure S4) showed an increase in lateral film growth rates that commensurate to the increase in the thermodynamic driving force but with plateau regions. Since gas hydrates typically had high heat of formation [43], as the degree of subcooling (ΔT_{sub}) increased, the experimental lateral growth rate was anticipated to increase. However, the trends plateau regions in trends of lateral growth rate were unexpected.

We examined the trends of observed lateral Xe hydrate film growth by categorizing the different temperature growth zones within these trends and correlating these zones to our calculations of net Xe flux to the water films in section mass transfer processes: Net mass flux and aqueous solubility of Xe. For the experiments under 2.75 bar of Xe, three temperature growth zones were identified (Figure 6a). In zone I, at a low degree of subcooling when the net flux of Xe and solubility of Xe in the water film were low, the lateral growth rate was observed to increase significantly by more than five times when ΔT_{sub} increased from 19 to 22 K. However, in zone II, the lateral growth rate had little changes when ΔT_{sub} increased from 22 to 29 K.

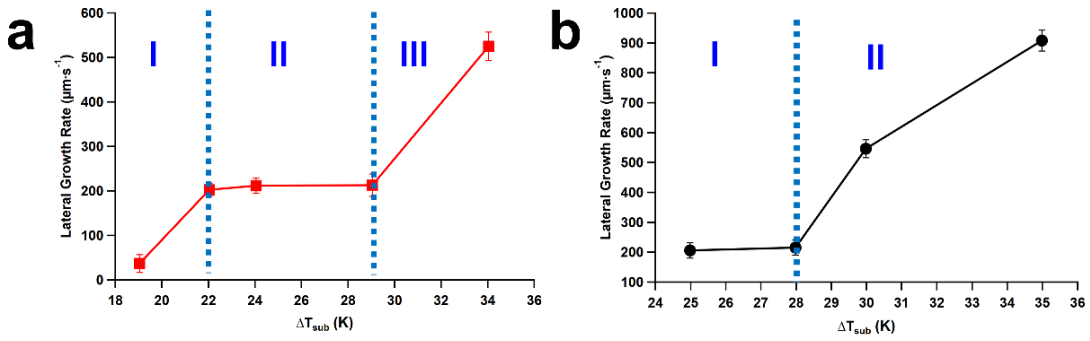

Figure 6. Plots of the lateral growth rate of Xe hydrate films vs. degree of subcooling (ΔT_{sub}), under (a) P_{exp} = 2.75 bar and (b) P_{exp} = 3.45 bar of Xe. The error bars show one standard deviation of the measurements.

In zone III, as ΔT_{sub} increased from 29 to 34 K, a higher degree of subcooling when the net mass flux of Xe and the solubility of Xe in the water film were much higher, the increase in the lateral growth rate resumed much sharper than the case as in zone I. The plateau region (zone II) in the double-sigmoid-like trend was only noticeable when the net mass flux of Xe was low around intermediate subcooling temperatures and the supply of Xe to the film became the rate-limiting factor. These observations suggested that, besides the thermodynamic driving force parameters (ΔT_{sub} and ΔP_{sup}), another favorable driving force factor for the lateral growth of Xe hydrate film could be present in our study system. However, as the degree of subcooling increased further, the net mass flux of Xe increased overwhelmingly, hence, making the promoting effect of this factor too weak to stand out in zone III. In contrast, the trend of the lateral film growth rate under 3.45 bar of Xe demonstrated only a sigmoid curve with two growth zones (Figure 6b). The plateau region was at the beginning of the studied range of subcooling temperatures in the zone I, followed by a region with a

rapid increase in lateral growth rate in zone II. The lack of an initial growth zone with a considerable lateral growth rate increase in this trend was probably because ΔT_{sub} started with a much higher value (25 K) than that of the experiments under 2.75 bar of Xe (19 K). In addition, the net mass flux of Xe was significantly and sufficiently higher to sustain the increasing lateral growth rate in this case. This increase in reaction rate at lower temperatures may seem counter-intuitive because the chemical reactivity of molecules is typically reduced at low temperatures and hence the reaction is slowed down. However, a simple thermodynamic analysis reveals that the formation of gas hydrates is favorable at low temperatures. The heat of formation for Xe hydrate is negative ($\Delta H_{reaction}$ = −30.8 kJ/mol) [42]. When Xe is trapped in a hydrate cage structure, the heat of intercalation is −22.4 kJ/mol [38,42]. Since gas and water molecules are trapped in solid gas hydrate structures, the change in entropy in this gas hydrate formation process ($\Delta S_{reaction}$) is also negative. The change in Gibbs free energy of the hydrate formation ($\Delta G_{reaction}$) is equal to $\Delta H_{reaction} - T \cdot \Delta S_{reaction}$, where T is the reaction temperature. Thus, since both $\Delta H_{reaction}$ and $\Delta S_{reaction}$ are negative, if we assume that both terms do not change much in a small temperature range (<20 K). $\Delta G_{reaction}$ will become more negative as the reaction temperature (T) decreases. Consequently, the gas hydrate formation will also become more thermodynamically favorable. In addition, since our hydrate formation system is an open system, other factors such as mass transfer also play important roles in driving the reaction forward. Through our net mass transfer calculations, we observed that as the degree of subcooling increased, the calculated net mass flux of Xe increased and so did the mole fraction of Xe. Thus, both thermodynamic analysis and mass transfer estimation predicted the high lateral growth rate observed at a higher degree of subcooling.

The plots of the lateral film growth rate of Xe hydrate versus superpressure (ΔP_{sup}) revealed the lateral growth rate trends to be similar to the ones plotted against ΔT_{sub} (Figure S4 in supplementary). ΔP_{sup} signified the parameter that described the driving force behind the transfer of Xe between the gas/liquid and the gas/solid interfaces. As ΔT_{sub} increased with a rise in ΔP_{sup}, the supply of Xe to the water films increased correspondingly. Under both Xe pressure conditions in our study, the v_f again generally increased with the increasing degree of superpressure.

Apart from studies on lateral growth of films, reports focusing on measuring the hydrate film thickness or thickness growth rate of hydrate films are limited and intermittently reported. In the past, the hydrate films thickness has been studied using micrometry, microscopy, laser interferometry, and magnetic resonance imaging (MRI). However, all these techniques had their limitations. For instance, visual techniques such as micrometry and microscopy are only applicable when attached with a suitable high-pressure reaction cell having transparent windows are used. These cells are expensive and cannot be used to study larger systems [36]. The major drawback of visual techniques for studying film thickness rate is that it can only be used to observe the sample area which is in contact with the transparent window while the rest of the sample is off-limit. To overcome the limitation of visual methods, Ohmura et al. [44] reported the first study to measure the hydrate film thickness rate using laser interferometry. The working principle behind this technique was when a laser is focused on the hydrate film, the reflected rays produced a unique pattern (interferogram) on a screen through which the hydrate film thickness could be determined. This technique was successful for low subcooling conditions; however, at larger subcooling temperatures, the hydrate film was coarse and had a rough texture. In this case, the interferogram generated was not clear and hard to decipher. Hence, both visual and interferometry techniques are unfit for hydrate films formed using a liquid (water or hydrate forming agent) droplet or a gas bubble. Following this, the MRI method was

proposed by Hirai et al. [45] in which MRI could detect only the water phase not the crystalline phase of the hydrate film. The authors used MRI to study hydrate film formed by a water droplet in liquid CO_2. Their experiment showed that CO_2 hydrate film thickness increased 0.8 mm in 200 min and then reached a constant. However, the information regarding the initial thickness of the CO_2 hydrate film couldn't be obtained. Recently, Liang et al. [46] applied X-ray computed tomography (XCT) to investigate the growth of Xe hydrate films on water droplets and achieved encouraging micron-scale detailed structures of hydrate growth. In principle, XCT could be potentially applied to evaluate many hydrate film parameters such as hydrate film morphology, porosity, film thickness, and film thickening rates. Nevertheless, XCT also has some intrinsic limitations which can cause "artifacts" in the data that can inhibit effective interpretation of the data [47–49]. The most common issue with XCT is the "beam-hardening artifact" that could be caused by non-linear polychromatic attenuation of X-ray which can diminish the XCT data quality by influencing the measurements related to porosity [50] and dimensional analysis [51]. Materials such as certain types of plastics with high attenuation contrast are also known to cause artifacts in XCT data acquisition and interpretation. While the use of XCT in material structure studies is a burgeoning field of research, its use in the investigations of hydrate growth remains underutilized due to its limited access to most hydrate researchers. Since determining the thickness of hydrate films and hence the rate of its increase have been technically challenging even in focused studies and are yet completely resolved, we did not pursue such measurements in our study.

3.4. Possible roles of the water-mica interface

We proposed that the lateral Xe hydrate film growth in our study was strongly promoted by the structures of water molecules templated on the surface of mica. Solid surfaces, particularly hydrophilic surfaces, are known to promote gas hydrate growth by providing nucleation sites [20,52,53]. However, there are yet no unified explanations for the reported film growth phenomena. In our case, as discussed above, the mica surface was composed of atomically flat silicate sheets decorated with metal ions (such as K^+) and these structures had been demonstrated to template water molecules to form an ice-like two-dimensional H-bonded network on the mica surface even at room temperature [28,54]. It is known that the structures of the water layer near the water-surface interface can be altered by the H-bonding environment within the water molecules [31,55]. Therefore, the structured water network at the hydrophilic surface of a substrate (mica) can critically govern the conformation and the density of the water molecules at the water-surface interface [31]. This ice-like arrangement of the interfacial water molecules probably lowered the energetics for hydrate film formation at the interface to promote the lateral film growth process at the growth front as illustrated by our observed fast lateral hydrate film growth rates in comparison to previously reported hydrate film studies (Figure 7) [36,41,56]. In addition, the observed nucleation of gas hydrates and their lateral film growth could also be governed by the degree of super-saturation across the interface that relies on thermodynamic conditions and the cross-solubility of different species [57]. The aqueous solubility of the gas former is also a major factor contributing to the hydrate growth process. The relatively high solubility of Xe in water (for example, 0.6 g per 100 mL of water at 293 K [58]) and Xe's high affinity to form clathrate hydrate structure together with the hydrate promoting effect of the hydrophilic mica surface were the main factors behind the fast growth kinetics of Xe hydrate observed in this study. These findings agreed

well with the literature where hydrophilic surfaces have been reported to promote bulk hydrate formation [52,59,60], further corroborating the proposed promoting roles of mica to induce fast lateral growth kinetics of Xe hydrate films.

Recent progress by modeling has shed light on the understanding of the effect of the hydrophilic interface on hydrate growth. For example, Bai et al. [61] applied molecular dynamics simulation to study the nucleation of carbon dioxide (CO_2) hydrate in a super-saturated CO_2 solution system on surfaces with different degrees of hydrophilicity. They found that on a crystalline hydrophilic surface (100%-OH group), water molecules at the water-surface interface arranged themselves in an ice-like manner, resulting in the formation of H-bonds widely different from the inherent water-water H-bonds in terms of strength and orientation. Notably, the ice-like arrangement was followed by an intermediary layer which was somewhat a hybrid between ice-like arrangement and CO_2 hydrate structure. This intermediary structure then finally yielded a stable CO_2 hydrate layer, further suggesting that surfaces with ordered water structures can promote lateral hydrate film growth.

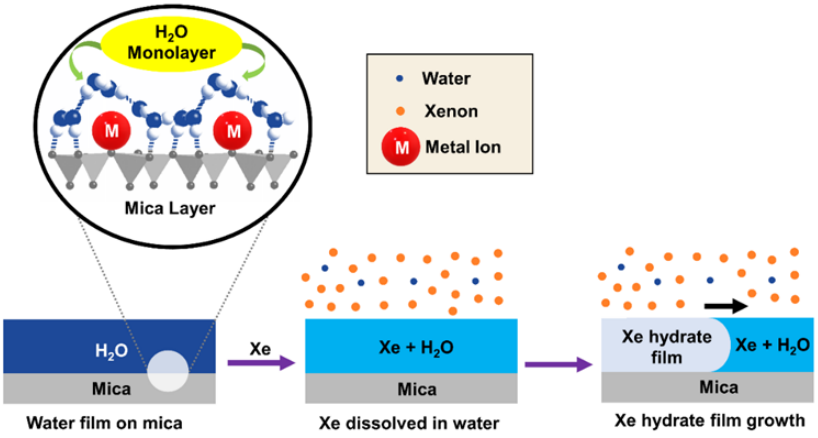

Figure 7. Schematic of a proposed lateral growth mechanism for a Xe hydrate film on mica. (Inset) Structure of water monolayer formed on mica surface. Reproduced with permission from ref. [28].

Based on our discussed hypotheses, we attributed our observed trends of the Xe hydrate lateral film growth to the interplay of several factors: (1) high formation energy required to form the hydrate films; (2) thermodynamic driving force (ΔT_{sub} and ΔP_{sup}) in the experiments; (3) net flux of Xe to the films; (4) the solubility of Xe in the water films at the experimental temperatures, and (5) the promotional surface effect of mica on the lateral film growth. At a low degree of subcooling, even with a relatively low net flux of Xe, the hydrophilic nature of mica could have affected the local organization of water molecules near the liquid-solid interfaces [20] on the surface and lower the energetics to favor the lateral hydrate film growth at the growth front. This was indirectly reflected by the short induction time of the hydrate films. However, this increase in the lateral hydrate growth rate could pause and level off as the lateral growth of hydrate film was limited by the availability of Xe from the water film. At a much high degree of subcooling when the net flux of Xe and the solubility of Xe in the water film were high, the larger net mass flux and driving force could re-enable and enhance the lateral hydrate growth while the surface effect became less unnoticeable at a high growth rate. Note that many lateral growth models of hydrate films that used the convective

heat transfer concept had been proposed to describe unsupported hydrate films over the past decade [36]. Particularly, a hydrate film growth model that predicted an exponential relationship between the lateral growth rate and the subcooling temperature ($v_f \propto \Delta T_{sub}^{5/2}$) had been successfully applied to describe the lateral growth of hydrate films on the surface of liquid-water droplets suspended in the air [62] with excellent goodness of fit. However, while this formula successfully describes the general concave-upward trend of hydrate lateral film growth in the literature and our study, none of this and other similar models applied to our study because they do not include parameters that described surface effects on the film growth.

4. Conclusion

We studied the lateral growth of Xe hydrate films on mica at sub-zero temperatures under two superpressure conditions and proposed a hypothesis to explain the plateau feature in the observed trend of lateral film growth rates versus the thermodynamic driving force parameters. Our results revealed that the Xe hydrate films formed at very fast average lateral growth rates (~200–400 μm/s) in contrast to other reported gas hydrate films which take hours to form [63]. The response of the lateral film growth rates on mica to the increasing degree of superpressure and subcooling as well as the reported water structures at the mica-water interface from experiments and modeling were used to construct a hypothesis to explain the trend of fast lateral film growth. The estimated low net mass flux of Xe to the water film at the gas/water interface and its aqueous solubility at a small degree of subcooling indirectly hinted that the mica surface possibly assisted the lateral growth process of Xe hydrate films at the growth front when the net mass flux of Xe and the solubility of Xe in the water film were limited. However, this trend of lateral film growth plateaued when the growth rate superseded the limited supply of Xe from the water film. The lateral film growth rate resumed to take off again when the degree of subcooling was sufficiently high enough to increase the mass flux and solubility of Xe to the water film. The proposed surface-promotional effect observed for lateral film growth of Xe hydrate at the growth front was ascribed to the structured-water network at the metal ions decorated surface of mica and the arrangement of the basal oxygens of the silicate sheet.

Acknowledgments

The authors thank the National Science Foundation (Grant#: CHE 1665324) for financial support. We are grateful to Dr. Alexander Sinitskii for access to the confocal micro-Raman microscope.

Conflicts of interest

The authors declare no conflicts of interest.

References

1. Koh CA, Sloan ED, Sum AK, et al. (2011) Fundamentals and applications of gas hydrates. *Annu Rev Chem Biomol* 2: 237–257.
2. Both AK, Gao Y, Zeng XC, et al. (2021) Gas hydrates in confined space of nanoporous materials: new frontier in gas storage technology. *Nanoscale* 13: 7447–7470.

3. Koh CA, Sum AK, Sloan ED (2009) Gas hydrates: Unlocking the energy from icy cages. *J Appl Phys* 106: 061101.
4. Max MD (2003) *Natural Gas Hydrate in Oceanic and Permafrost Environments*, Dordrecht, Netherlands: Kluwer Academic Publishers.
5. Miller SL (1961) The occurence of gas hydrates in the solar system. *P Natl Acad Sci USA* 47: 1798.
6. Gudipati MS, Castillo-Rogez J (2012) *The Science of Solar System Ices*, New York, USA: Springer Science & Business Media.
7. Chong ZR, Yang SHB, Babu P, et al. (2016) Review of natural gas hydrates as an energy resource: Prospects and challenges. *Appl Energy* 162: 1633–1652.
8. Kargel JS, Lunine JI (1998) Clathrate hydrates on earth and in the solar system. In: Schmitt B, De Bergh C, Festou M, *Solar System Ices*. Dordrecht, Netherlands: Springer, 97–117.
9. Fu X, Waite WF, Cueto-Felgueroso L, et al. (2019) Xenon hydrate as an analog of methane hydrate in geologic systems out of thermodynamic equilibrium. *Geochem Geophy Geosy* 20: 2462–2472.
10. Kobelev A, Yashin V, Penkov N, et al. (2019) An optical microscope study of the morphology of xenon hydrate crystals: Exploring new approaches to cryopreservation. *Crystals* 9: 215.
11. Shishova NV, Fesenko EE (2015) The prospects of the application of gases and gas hydrates in cryopreservation. *Biophysics* 60: 782–804.
12. Mousis O, Lunine JI, Picaud S, et al. (2010) Volatile inventories in clathrate hydrates formed in the primordial nebula. *Faraday Discuss* 147: 509–525.
13. Owen T, Bar-Nun A, Kleinfeld I (1992) Possible cometary origin of heavy noble gases in the atmospheres of Venus, Earth and Mars. *Nature* 358: 43–46.
14. Shcheka SS, Keppler H (2012) The origin of the terrestrial noble-gas signature. *Nature* 490: 531–534.
15. Kvamme B, Aromada SA, Saeidi N, et al. (2020) Hydrate nucleation, growth, and induction. *ACS Omega* 5: 2603–2619.
16. Kvamme B, Zhao J, Wei N, et al. (2020) Hydrate—A mysterious phase or just misunderstood? *Energies* 13: 880.
17. Broseta D, Ruffine L, Desmedt A (2017) *Gas Hydrates 1: Fundamentals*, *Characterization and Modeling*, Hoboken, NJ, USA: John Wiley & Sons.
18. Ma R, Zhong H, Li L, et al. (2020) Molecular insights into the effect of a solid surface on the stability of a hydrate nucleus. *J Phys Chem C* 124: 2664–2671.
19. Aman ZM, Koh CA (2016) Interfacial phenomena in gas hydrate systems. *Chem Soc Rev* 45: 1678–1690.
20. Nguyen NN, Galib M, Nguyen AV (2020) Critical review on gas hydrate formation at solid surfaces and in confined spaces—Why and how does interfacial regime matter? *Energ Fuel* 34: 6751–6760.
21. Shen YR, Ostroverkhov V (2006) Sum-frequency vibrational spectroscopy on water interfaces: polar orientation of water molecules at interfaces. *Chem Rev* 106: 1140–1154.
22. You K, Flemings PB, Malinverno A, et al. (2019) Mechanisms of methane hydrate formation in geological systems. *Rev Geophys* 57: 1146–1196.
23. Deer WA, FRS, Howie RA, Zussman J (2013) *An Introduction to the Rock-Forming Minerals*, London, UK: Mineralogical Society of Great Britain and Ireland.

24. Nguyen AN, Zinner E (2004) Discovery of ancient silicate stardust in a meteorite. *Science* 303: 1496.
25. Messenger S, Keller LP, Stadermann FJ, et al. (2003) Samples of stars beyond the solar system: silicate grains in interplanetary dust. *Science* 300: 105.
26. de Poel W, Pintea S, Drnec J, et al. (2014) Muscovite mica: Flatter than a pancake. *Surf Sci* 619: 19–24.
27. Fukuma T, Ueda Y, Yoshioka S, et al. (2010) Atomic-scale distribution of water molecules at the mica-water interface visualized by three-dimensional scanning force microscopy. *Phys Rev Lett* 104: 016101.
28. Odelius M, Bernasconi M, Parrinello M (1997) Two dimensional ice adsorbed on mica surface. *Phys Rev Lett* 78: 2855–2858.
29. Bluhm H, Inoue T, Salmeron M (2000) Formation of dipole-oriented water films on mica substrates at ambient conditions. *Surf Sci* 462: L599–L602.
30. Miranda PB, Xu L, Shen YR, et al. (1998) Icelike water monolayer adsorbed on mica at room temperature. *Phys Rev Lett* 81: 5876–5879.
31. Cheng L, Fenter P, Nagy KL, et al. (2001) Molecular-scale density oscillations in water adjacent to a mica surface. *Phys Rev Lett* 87: 156103.
32. Peng BZ, Dandekar A, Sun CY, et al. (2007) Hydrate film growth on the surface of a gas bubble suspended in water. *J Phys Chem B* 111: 12485–12493.
33. Ballard AL, Sloan ED (2004) The next generation of hydrate prediction: Part III. Gibbs energy minimization formalism. *Fluid Phase Equilibr* 218: 15–31.
34. Lang C, Zhao J, Yuan C, et al. (2019) Growth patterns of xenon hydrate on surfaces with varying wettability. *International Conference on Applied Energy 2019*.
35. Khurana M, Yin Z, Linga P (2017) A review of clathrate hydrate nucleation. *ACS Sustain Chem Eng* 5: 11176–11203.
36. Sun CY, Peng BZ, Dandekar A, et al. (2010) Studies on hydrate film growth. *Annu Rep Prog Chem, Sect C: Phys* 106: 77–100.
37. Fray N, Marboeuf U, Brissaud O, et al. (2010) Equilibrium data of methane, carbon dioxide, and xenon clathrate hydrates below the freezing point of water. Applications to astrophysical environments. *J Chem Eng Data* 55: 5101–5108.
38. Sanloup C, Mao H-k, Hemley RJ (2002) High-pressure transformations in xenon hydrates. *P Natl Acad Sci USA* 99: 25.
39. Sugahara K, Sugahara T, Ohgaki K (2005) Thermodynamic and Raman spectroscopic studies of Xe and Kr hydrates. *J Chem Eng Data* 50: 274–277.
40. Carey DM, Korenowski GM (1998) Measurement of the Raman spectrum of liquid water. *J Chem Phys* 108: 2669–2675.
41. Nagashima HD, Oshima M, Jin Y (2020) Film-growth rates of methane hydrate on ice surfaces. *J Cryst Growth* 537: 125595.
42. Barrer RM, Edge AVJ (1967) Gas hydrates containing argon, krypton and xenon: kinetics and energetics of formation and equilibria. *Proc R Soc Lond A* 300: 1–24.
43. Cox JL (1983) *Natural Gas Hydrates: Properties, Occurrence and Recovery*. USA: Butterworth.
44. Ohmura R, Kashiwazaki S, Mori YH (2000) Measurements of clathrate-hydrate film thickness using laser interferometry. *J Cryst Growth* 218: 372–380.

45. Hirai S, Tabe Y, Kuwano K, et al. (2000) MRI measurement of hydrate growth and an application to advanced CO_2 sequestration technology. *Ann Ny Acad Sci* 912: 246–253.
46. Liang H, Guan D, Shi K, et al. (2022) Characterizing mass-transfer mechanism during gas hydrate formation from water droplets. *Chem Eng J* 428: 132626.
47. Sun W, Brown S, Leach R (2012) An overview of industrial X-ray computed tomography. *NPL Report ENG 32*.
48. Wilson P, Williams MA, Warnett JM, et al. (2017) Utilizing X-ray computed tomography for heritage conservation: The case of Megalosaurus bucklandii. *2017 IEEE International Instrumentation and Measurement Technology Conference*.
49. Wilson PF, Smith MP, Hay J, et al. (2018) X-ray computed tomography (XCT) and chemical analysis (EDX and XRF) used in conjunction for cultural conservation: the case of the earliest scientifically described dinosaur Megalosaurus bucklandii. *Herit Sci* 6: 58.
50. Hermanek P, Carmignato S (2016) Reference object for evaluating the accuracy of porosity measurements by X-ray computed tomography. *Case Stud Nondestruct Test Eval* 6: 122–127.
51. Lifton JJ, Malcolm AA, McBride JW (2015) An experimental study on the influence of scatter and beam hardening in X-ray CT for dimensional metrology. *Meas Sci Technol* 27: 015007.
52. Esmail S, Beltran JG (2016) Methane hydrate propagation on surfaces of varying wettability. *J Nat Gas Sci Eng* 35: 1535–1543.
53. Guo Y, Xiao W, Pu W, et al. (2018) CH_4 nanobubbles on the hydrophobic solid-water interface serving as the nucleation sites of methane hydrate. *Langmuir* 34: 10181–10186.
54. Bai D, Chen G, Zhang X, et al. (2015) How properties of solid surfaces modulate the nucleation of gas hydrate. *Sci Rep* 5: 12747.
55. Buch V, Devlin JP (2003) *Water in Confining Geometries*. New York, USA: Springer Science & Business Media.
56. Striolo A, Phan A, Walsh MR (2019) Molecular properties of interfaces relevant for clathrate hydrate agglomeration. *Curr Opin Chem Eng* 25: 57–66.
57. Both AK, Cheung CL (2019) Growth of carbon dioxide whiskers. *RSC Adv* 9: 23780–23784.
58. Kennan RP, Pollack GL (1990) Pressure dependence of the solubility of nitrogen, argon, krypton, and xenon in water. *J Chem Phys* 93: 2724–2735.
59. He Z, Linga P, Jiang J (2017) CH_4 hydrate formation between silica and graphite surfaces: insights from microsecond molecular dynamics simulations. *Langmuir* 33: 11956–11967.
60. He Z, Mi F, Ning F (2021) Molecular insights into CO_2 hydrate formation in the presence of hydrophilic and hydrophobic solid surfaces. *Energy* 234: 121260.
61. Bai D, Chen G, Zhang X, et al. (2011) Microsecond molecular dynamics simulations of the kinetic pathways of gas hydrate formation from solid surfaces. *Langmuir* 27: 5961–5967.
62. Mori YH (2001) Estimating the thickness of hydrate films from their lateral growth rates: application of a simplified heat transfer model. *J Cryst Growth* 223: 206–212.
63. Takeya S, Hachikubo A (2019) Structure and density comparison of noble gas hydrates encapsulating Xenon, Krypton and Argon. *ChemPhysChem* 20: 2518–2524.

AIMS Press

© 2021 the Author(s), licensee AIMS Press. This is an open access article distributed under the terms of the Creative Commons Attribution License (http://creativecommons.org/licenses/by/4.0)